Infrared dynamics of cold atoms on hot graphene membranes

Sanghita Sengupta, Valeri N. Kotov, and Dennis P. Clougherty
Department of Physics, University of Vermont, Burlington, Vermont 05405-0125, USA
(Received 4 April 2016; published 21 June 2016)

We study the infrared dynamics of low-energy atoms interacting with a sample of suspended graphene at finite temperature. The dynamics exhibits severe infrared divergences order by order in perturbation theory as a result of the singular nature of low-energy flexural phonon emission. Our model can be viewed as a two-channel generalization of the independent boson model with asymmetric atom-phonon coupling. This allows us to take advantage of the exact nonperturbative solution of the independent boson model in the stronger channel while treating the weaker one perturbatively. In the low-energy limit, the exact solution can be viewed as a resummation (exponentiation) of the most divergent diagrams in the perturbative expansion. As a result of this procedure, we obtain the atom's Green function which we use to calculate the atom damping rate, a quantity equal to the quantum sticking rate. A characteristic feature of our results is that the Green's function retains a weak, infrared cutoff dependence that reflects the reduced dimensionality of the problem. As a consequence, we predict a measurable dependence of the sticking rate on graphene sample size. We provide detailed predictions for the sticking rate of atomic hydrogen as a function of temperature and sample size. The resummation yields an enhanced sticking rate relative to the conventional Fermi golden rule result (equivalent to the one-loop atom self-energy), as higher-order processes increase damping at finite temperature.

DOI: 10.1103/PhysRevB.93.235437

I. INTRODUCTION

The study of the dynamics of cold atoms near suspended graphene samples presents opportunities to explore some of the foundational concepts of quantum mechanics. Since the binding energy of an atom on graphene is comparable to graphene's quantum excitation energies, the dynamics depends on a quantum treatment of excitations. Even the atomic motion must be treated quantum mechanically for sufficiently cold atoms. Thus the theory of cold atom adsorption on graphene must be a fully quantum theory.

From a practical perspective, information gleaned from dynamical studies of cold atoms near surfaces will likely find use in the development and refinement of systems and devices for quantum sensing and information processing. In recent years, there have been many experimental advances in the cooling and control of atoms and molecules. Picokelvin sources of helium atoms can now be experimentally prepared [1], and new technologies propose to use quantum states of cold atoms and molecules to store and process information [2,3]. One example of these potential applications is realized in the "atom chip," a microelectronic device where currents flowing through nanowires generate magnetic fields to process information stored in the quantum states of cold atoms.

A second example is in quantum metrology. This includes applications such as recently developed chip-scale atomic clocks using cold ^{87}Rb atoms [4]. The operation of these devices will be strongly impacted [5] by how cold atoms and molecules interact with surfaces. Hence our theoretical studies will impact performance and design of these emerging applications; for example, unintended adsorption of alkali metal atoms leads to the so-called "patch effect," where random islands of dipoles can cause a rapid dephasing of entangled states of atoms trapped above surfaces.

Another potential application is in "atom optics" where matter waves play the role conventionally performed by laser light in optical systems [6]. Enhancing the reflection of matter waves from surfaces might be used to make low-loss atomic mirrors [7], wave guides for atom interferometers [6] or microtraps for the quantum information processing of cold atoms [8].

Research in the field of cold atom-surface interactions traces back to the beginning years of quantum theory, where the threshold behavior for quantum adsorption was first explored by Lennard-Jones [9]. Early theoretical work concluded that the sticking probability $s(E)$ of a particle with incident energy E near threshold is directly proportional to the square of the transition matrix element and varies inversely with the incident particle flux, such that $s(E) \propto \sqrt{E}$. More recent studies [10–12] have predicted new scaling laws for neutral and charged particles based on quantum many-body effects, such as orthogonality catastrophe-type phenomena.

For inelastic interactions, the primary channel of energy exchange involves the creation and annihilation of phonons. Free-standing graphene has two in-plane acoustic modes and one out-of-plane flexural mode. The flexural mode has a quadratic dispersion near the zone center; however, under uniform tension, the flexural dispersion becomes linear, leading to vanishing phonon density of states (DOS) for suspended graphene. In contrast to a constant DOS at zero frequency, a linear DOS eases a well-known divergence in the displacement autocorrelation function of the nth nearest neighbors $\langle (u_n - u_0)^2 \rangle$ in two dimensions [13] and stabilizes the suspended layer mechanically, circumventing the "crumpling" instability. In the case of inelastic atom-graphene interactions, vestiges of this divergence can be found in a perturbative expansion of the atom's self-energy [14]. The linear DOS of the flexural phonons, when combined with the frequency-dependent atom-phonon coupling gives a (log) divergent atom self-energy at zero temperature. This implies that without a low-frequency cutoff, the second-order shift in the binding energy of a light atom on suspended graphene is formally divergent [14]. Recent numerical calculations on the physisorption of atomic hydrogen to suspended graphene [15]

do not take into account the effect of this infrared divergence which remains a theoretical challenge.

In the present paper, we use a diagrammatic approach to study the dynamics of quantum sticking near graphene membranes. The quantum sticking probability is related to the damping rate of the atom, calculated from its self-energy. In fact, the study of atom self-energy to probe various aspects of atom-surface scattering is not a recent one and has been explored before [16–18]. The presence of infrared divergent terms, due to many emitted low-energy flexural phonons, has been previously pointed out [14,19], and our goal in this paper is to provide a systematic study of these effects in the context of renormalized perturbation theory.

We will consider membranes at finite temperature T, where the infrared divergence problem is especially severe since the number of thermally-activated phonons tends to infinity with increasing membrane size. However, there is a well-defined way to take into account (through resummation) such infrared-singular processes; especially suggestive is an exact solution for a particle (atom) interacting with a bath of phonons (independent boson model [20]), even though our problem is not exactly solvable in the same sense due to the presence of two types of atom-phonon couplings [19].

Quite remarkably, the problem under consideration is also technically similar to the infrared problems present in finite-T "hot" quantum electrodynamics (QED) and quantum chromodynamics (QCD) due to the long-range, unscreened, nature of gauge interactions [21–24]. These problems are usually resolved within the finite T generalization of the so-called Bloch-Nordsieck scheme [21,22], which extracts the exact infrared behavior of the theory by summing the most important Feynman diagrams; it is quite similar to the exact solution of the independent boson model (IBM) for single atom-phonon bath mentioned previously. Physically this corresponds to the correct account of the damping provided by many emitted phonons, and we will implement similar schemes to obtain the sticking rate of adatoms (equivalent to calculating the atomic damping rate).

Since the infrared divergences are caused by emitted low-momentum phonons $q \to 0$, at any finite-T around the Debye temperature, the system is effectively in the high temperature (hot) limit as far as its infrared properties are concerned, $T \gg v_s q$, where v_s is the flexural phonon speed. Similar to the case of hot QED, this allows for a particularly theoretically clean and elegant way to perform resummation of the leading infrared divergences which come as powers of logarithms.

We present a detailed study of the atomic self-energy at one and two loops, and subsequently perform resummation of the leading infrared terms in the spirit of the IBM or hot QED, but adapted for our two-channel situation. This allows us to obtain reliable nonperturbative results for the damping rate as a function of temperature (T) as well as membrane size (L), which serves as the effective infrared cutoff in the problem. The description of these dependencies and the theoretical methodology we use to calculate them is the main goal of this work.

The rest of the paper is organized as follows. In Sec. II, we introduce the effective model of atoms interacting with graphene membranes. In Sec. III, we analyze the infrared divergences that appear up to two loops and then present the nonperturbative solution in the spirit of the IBM in Sec. IV. Our results for a H atom's sticking rate as a function of temperature and size are collected in Sec. V. Section VI contains our conclusions. Some technical aspects of high-order perturbation theory are presented in Appendices A and B.

II. MODEL OF COLD ATOMS ON GRAPHENE MEMBRANE AT FINITE TEMPERATURE

We study the interaction of a cold atom with a clamped, elastic membrane (Fig. 1), where the inelastic interaction between the atom and the membrane occurs through the creation and annihilation of flexural phonons of the membrane. For atoms focused near the center of the suspended membrane, the circularly symmetric modes dominate the inelastic scattering. Thus we consider the atom interactions with only the axisymmetric ($m = 0$) modes [19].

The Hamiltonian of the system is written as $H = H_p + H_{ph} + H_c$. The terms represent the Hamiltonian for the particle, phonon-bath, and the coupling term, respectively, and are given as:

$$H_p = E_k c_k^\dagger c_k - E_{b0} b^\dagger b \tag{1}$$

$$H_{ph} = \sum_q \omega_q a_q^\dagger a_q \tag{2}$$

$$H_c = -g_{kb}(c_k^\dagger b + b^\dagger c_k)\sum_q \xi_q (a_q + a_q^\dagger) - g_{bb} b^\dagger b \sum_q \xi_q (a_q + a_q^\dagger). \tag{3}$$

Here, c_k ($c_k^\dagger$) annihilates (creates) a particle in the entrance channel $|k\rangle$ with energy E_k; b ($b^\dagger$) annihilates (creates) a particle in the bound state $|b\rangle$ with energy $-E_{b0}$ in the potential of a static membrane in its initial equilibrium position; a_q ($a_q^\dagger$) annihilates (creates) a phonon in the membrane with energy ω_q; g_{kb} is the coupling strength of phonon-assisted transitions of the atom between continuum $|k\rangle$ and bound state $|b\rangle$; g_{bb} is the coupling strength of the bound atom to flexural phonons. The form of ξ_q depends on the specific particle-excitation coupling, and particularly in this model, ξ_q is q independent [19].

We take the membrane to be initially in thermal equilibrium with temperature T, while the atoms have an initial

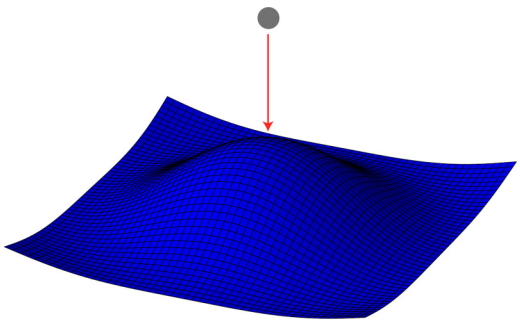

FIG. 1. Sketch of the membrane with an impinging atom. The membrane distorts from its initial equilibrium plane with the presence of the adatom.

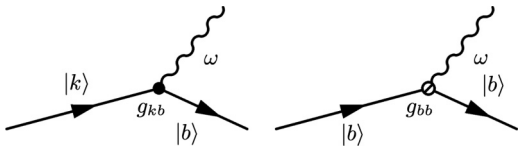

FIG. 2. Feynman diagrams with two kinds of vertices: transition of atom from $|k\rangle$ to $|b\rangle$ state via a phonon has vertex g_{kb} (left), and atom-phonon interaction in the bound state $|b\rangle$ has vertex g_{bb} (right).

energy of E_k. The atom self-energy must be calculated using nonequilibrium Green functions (Keldysh or the contour-ordered Green functions). The Feynman rules, see Fig. 2, using the Keldysh formalism are summarized below for our model:

(i) The solid dot corresponds to the interaction vertex g_{kb}.

(ii) The open dot corresponds to the interaction vertex g_{bb}.

(iii) Lines labeled by b correspond to the bare (retarded) Green function in the bound state $G^r_{bb}(E) = 1/(E + E_{b0} + i\eta)$.

(iv) Lines labeled by k correspond to the bare (retarded) Green function of the atom in the continuum state $G^r_{kk}(E) = 1/(E - E_k + i\eta)$.

(v) Wiggly lines correspond to the phonon propagators and are given as:
$D^<(\omega) = -2\pi i \sum_q [(N_q + 1)\delta(\omega + \omega_q) + N_q \delta(\omega - \omega_q)]$
and $D^r(\omega) = \sum_q [1/(\omega - \omega_q + i\delta) - 1/(\omega + \omega_q + i\delta)]$. Here, N_q is the equilibrium phonon occupation number $N_q = 1/(e^{\beta\omega_q} - 1)$, and $\omega_q = v_s q$ for a membrane under tension.

(vi) Each diagram is weighted by $(i/\hbar)^n$, where n is the number of phonon loops.

Two additional comments are in order. First, we also assume that, by definition, the ground state is the initial (symmetric) vacuum of the phonons. It is possible that at low temperature, the phonons could condense, leading to finite membrane displacement and a symmetry-broken state; such a scenario was considered previously by one of us within a mean-field theory approach applied to this model [19]. The present study cannot shed light on that result, since we aim to collect the leading infrared-divergent terms that happen essentially in the "high-temperature" regime ($T \gg v_s q$, and $T > E_b$), and we are under the (well-satisfied) weak-coupling condition $\frac{g^2}{E_b} \ll 1$ (and $\frac{g^2 T}{E_b^2} \ll 1$), where g^2 is either g^2_{kb} or g^2_{bb}, with dimension of energy when appropriately written (see below). Under these assumptions, a perturbative expansion around the symmetric vacuum seems well justified; however, we certainly cannot rule out the possibility of symmetry breaking.

Finally, we mention that the diagram technique constructed above is completely equivalent to simply working with the real-time finite temperature Green's function for the phonons [20,25]. This can be easily seen by examining the structure of the one-loop result Eq. (6) and the way it follows from Eq. (5). Furthermore, it is clear that for the purposes of extracting the leading, infrared-divergent logarithmic terms, it is sufficient to use the small momentum/high temperature limit of the phonon propagator in the form $D^<(\omega,q) = -2\pi i(T/\omega_q)[\delta(\omega + \omega_q) + \delta(\omega - \omega_q)]$.

III. INFRARED-DIVERGENT SELF-ENERGIES AT LOW ORDERS

A. 1-loop atom self-energy

Applying the above Feynman rules, we find the finite temperature atom self-energy at the 1-loop level is given by

$$\Sigma^{(r)}_{kk}(E) = i \int \frac{d\omega}{2\pi} \sum_q g^2_{kb}\xi^2 [G^<_{bb}(E) D^r(\omega) + G^r_{bb}(E) D^<(\omega) + G^r_{bb}(E) D^r(\omega)]. \quad (4)$$

Since we take the incoming particle to be out of equilibrium with the phonon bath with the Green function $G^<_{bb}(E) = 0$, we obtain:

$$\Sigma^{(r)}_{kk}(E) = i \int \frac{d\omega}{2\pi} \sum_q g^2_{kb}\xi^2 \left[G^r_{bb}(E) D^<(\omega) + G^r_{bb}(E) D^r(\omega)\right] = g^2_{kb}\xi^2 \sum_q \left[\frac{N_q}{E + E_{b0} + \omega_q - i\eta} + \frac{N_q + 1}{E + E_{b0} - \omega_q + i\eta}\right]. \quad (5)$$

Next, in the continuum limit, we obtain the real and the imaginary part of $\Sigma^{(r)}_{kk}$ for the high temperature case ($T \gg \omega_D$, where ω_D is membrane Debye frequency). In this high temperature limit, we approximate $N_q \approx T/q$ (we choose convenient units where the velocity of sound $v_s = 1$). Also, we consider the energy regime $T, \omega_D \gg E_b$, and call $g^2_{kb}\xi^2\rho_0 \to g^2_{kb}$, where ρ_0 is the (constant) vibrational density of states. From previous work [19], we take $\xi^2\rho_0 = 3.77 \times 10^{-5}$ Å^2/meV.

As a result, we conclude that the real and the imaginary parts are given as:

$$\mathrm{Re}\,\Sigma^{(r)}_{kk}(E) = \frac{2g^2_{kb}T}{E + E_{b0}} \log\left|\frac{E + E_{b0}}{\epsilon}\right|, \quad \epsilon \ll E + E_{b0} \quad (6)$$

$$\mathrm{Im}\,\Sigma^{(r)}_{kk}(E) = -\frac{\pi g^2_{kb} T}{E + E_{b0}}, \quad (7)$$

where ϵ is the infrared cutoff estimated to be the minimum phonon frequency, $\epsilon \sim v_s/L$, where L is the characteristic membrane size (radius), which will be a parameter in our model.

Although the imaginary part is completely finite, Eq. (6) shows that the real part of the finite temperature atom self-energy is log-divergent for infrared frequencies. A similar expression can be derived for the 1-loop bound state self-energy Σ_{bb} corresponding to a Feynman diagram similar to Fig. 3 with g_{kb} replaced with g_{bb}. The expressions for the real

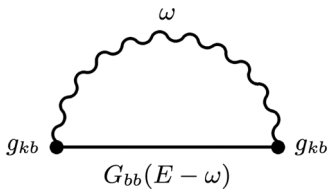

FIG. 3. One-loop atom self-energy $\Sigma^{(r)}_{kk}$.

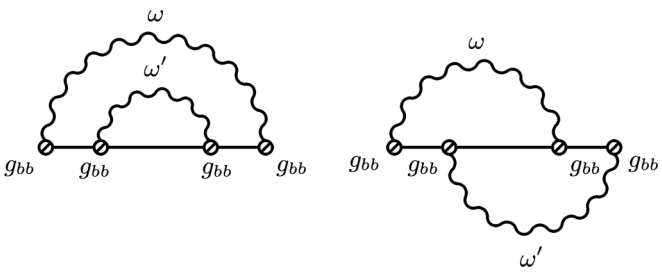

FIG. 4. Two-loop bound state self-energy diagrams. Left: nested (rainbow). Right: vertex correction.

and imaginary Σ_{bb} are given as:

$$\mathrm{Re}\Sigma^{(r)}_{bb}(E) = \frac{2g^2_{bb}T}{E+E_{b0}}\log\left|\frac{E+E_{b0}}{\epsilon}\right| \tag{8}$$

$$\mathrm{Im}\Sigma^{(r)}_{bb}(E) = -\frac{\pi g^2_{bb}T}{E+E_{b0}};\ E+E_{b0}\gg\epsilon. \tag{9}$$

The values of g_{bb} and g_{kb} depend on the form of the attractive (van der Waals) potential between the atom and the membrane; for a H atom impinging on suspended graphene, we will take them from previous work [19]. The coupling g_{kb} has a strong energy dependence, $g_{kb} = g_{kb}(E_k)$ where E_k is the atom's initial energy. This energy dependence will be taken into account in our final results. The coupling $g^2_{bb} = 60\ \mu$eV is independent of E_k, and in addition, is much larger than g^2_{kb} (for all E_k considered).

$$g^2_{bb} \gg g^2_{kb}. \tag{10}$$

The ratio of these couplings for an H atom is typically $g^2_{kb}/g^2_{bb} \sim 10^{-2}$. Because of this inequality, the bound state self-energy behavior in higher orders will be numerically much more important than the corresponding higher order contributions to the continuum self energy. Thus we first proceed to investigate the next order in powers of g^2_{bb}.

B. 2-loop bound state self-energy

We now turn to a calculation of the 2-loop bound state self-energy corresponding to the diagrams shown in Fig. 4. First, we evaluate the vertex correction diagram by using the vertex function $\Gamma(E,\omega)$ (see Fig. 5).

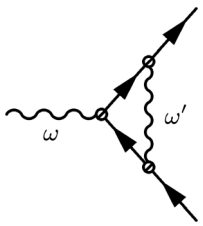

FIG. 5. Vertex function $\Gamma(E,\omega)$ to be inserted appropriately in Fig. 4 to derive the 2-loop bound state self-energy.

Following the Feynman rules, we find the following expression for $\Gamma(E,\omega)$

$$\Gamma(E,\omega) = ig^3_{bb}\xi^3\sum_q\int\frac{d\omega'}{2\pi}\frac{T}{\omega_q}(-2\pi i)\Big[\delta(\omega'-\omega_q) + \delta(\omega'+\omega_q)\Big]\times\Big[\frac{1}{[E+E_{b0}-\omega'+i\eta]} \times\frac{1}{[E+E_{b0}-\omega-\omega'+i\eta]}\Big]. \tag{11}$$

In the continuum limit, we call $g^2_{bb}\xi^2\rho_0 \to g^2_{bb}$, so that the real and the imaginary parts of the vertex function $\Gamma(E,\omega)$ are written as

$$\mathrm{Re}\Gamma(E,\omega) = \frac{2g^3_{bb}T}{(E+E_{b0})(E+E_{b0}-\omega)}\log\left|\frac{E+E_{b0}}{\epsilon}\right| \tag{12}$$

$$\mathrm{Im}\Gamma(E,\omega) = -\frac{\pi g^3_{bb}T}{(E+E_{b0})(E+E_{b0}-\omega)}. \tag{13}$$

Using Eqs. (12) and (13), we find the contribution to the vertex correction diagram. The analytical expression for Σ_{bb} is written as

$$\Sigma^{(2)}_{bb} = ig_{bb}\xi\int\frac{d\omega}{2\pi}G_{bb}(E-\omega)\Gamma(E,\omega)D^<(\omega). \tag{14}$$

Substituting, we conclude that the real part of $\Sigma^{(2)}_{bb}$ is given by

$$\mathrm{Re}\Sigma^{(2)}_{bb} = \frac{2g^4_{bb}T^2}{(E+E_{b0})^3}\left[\log\left|\frac{E+E_{b0}}{\epsilon}\right|\right]^2. \tag{15}$$

A similar expression can be easily obtained for the contribution from the rainbow diagram. Thus, the above calculations show that $\mathrm{Re}\Sigma_{bb}$ for both the 1-loop and the 2-loop is plagued by log and log-squared infrared divergences, respectively. Therefore, at the 2-loop level, $\mathrm{Re}\Sigma_{bb}(E)$ is given by

$$\mathrm{Re}\Sigma_{bb}(E) = \frac{2g^2_{bb}T}{E+E_{b0}}\log\left|\frac{E+E_{b0}}{\epsilon}\right| + 2\times\frac{2g^4_{bb}T^2}{(E+E_{b0})^3}\left[\log\left|\frac{E+E_{b0}}{\epsilon}\right|\right]^2+\ldots. \tag{16}$$

Given the above structure of the expansion, it is clear that in the infrared limit $(E+E_{b0})/\epsilon \gg 1$, resummation of the series must be performed to obtain reliable results. This turns out to be possible, and the infrared dynamics of the result is equivalent to that of the exact Green's function, $G_{bb}(E)$, of the independent boson model [20]. We can show that one can use Dyson's equation $G_{bb}(E) = G^{(0)}_{bb}(E)/(1-G^{(0)}_{bb}(E)\Sigma_{bb}(E))$, where $G^{(0)}_{bb}(E)$ and $\Sigma_{bb}(E)$ are the unperturbed bound state Green's function and the bound state self-energy, respectively, and then derive a perturbative expression for $G_{bb}(E)$ that matches exactly the perturbative structure of the exact bound state Green's function corresponding to the IBM. This is indeed natural since both the IBM and the part of our model involving bb transitions describe physically equivalent situations (a phonon bath coupled to a single particle).

With the presence of the second (kb) channel, our model can be viewed as a generalization of the IBM with two coupling constants g_{kb} and g_{bb}; however, due to the strong inequality Eq. (10), the infrared behavior originating from higher order processes in the kb channel is strongly suppressed and will be neglected. For example, one-loop (logarithmic) corrections to the b channel propagator due to mixing with the k channel are of order g_{kb}^2, much smaller than the pure bb channel contribution g_{bb}^2 calculated above. Thus the relative contribution of these processes is smaller by a factor of $g_{kb}^2/g_{bb}^2 \sim 10^{-2}$, based on calculations for H atom. Higher order processes are suppressed even stronger.

On the other hand we are ultimately interested in the Green's function of the k channel (Sec. V), and its dominant perturbative correction, as outlined in Appendix A, originates at order $g_{kb}^2 g_{bb}^2$. This is the dominant part in a sense that it is much larger than the pure mixing contribution of order g_{kb}^4, which can be neglected due to the same reasoning as above. Additional evidence in favor of this overall strategy is based on analysis of higher-order contributions to the two vertices, g_{kb}^2 and g_{bb}^2, as performed in Appendix B. We find that the effective vertex g_{bb}^2 grows, while g_{kb}^2 decreases under renormalization (i.e., upon including higher order singular corrections). These results provide further justification in favor of asymmetric treatment of the two couplings (channels) within the model. Thus we will follow the strategy of keeping the lowest necessary power of g_{kb}^2 while treating the bb channel nonperturbatively.

IV. BOUND STATE GREEN FUNCTION WITHIN THE INDEPENDENT BOSON MODEL

Based on the previous analysis we proceed to calculate the exact bb Green's function which will provide the dominant contribution to the atom damping rate, to be calculated in the next section. As already mentioned, if we consider only the bound state $|b\rangle$ contributions, we have the same Hamiltonian as that of the IBM:

$$H = -E_{b0} b^\dagger b + \sum_q \omega_q a_q^\dagger a_q - g_{bb} b^\dagger b \sum_q \xi_q (a_q + a_q^\dagger). \tag{17}$$

The exact Green's function $G_{bb}(t)$ corresponding to Eq. (17) is given as [20]:

$$G_{bb}(t) = -i e^{-it(-E_b)} e^{-\phi(t)}, \tag{18}$$

where

$$\phi(t) = \sum_q \left(\frac{g_{bb}\xi}{\omega_q}\right)^2 [N_q(1 - e^{i\omega_q t}) + (N_q + 1)(1 - e^{-i\omega_q t})] \tag{19}$$

and the binding energy E_b is defined $E_b = E_{b0} + g_{bb}^2 \sum_q \frac{1}{\omega_q}$, shifted by the phonon interaction.

In the high temperature approximation, Eq. (19) then becomes

$$\phi(t) = \sum_q \frac{2 g_{bb}^2 \xi^2}{q^2} \frac{T}{q} [1 - \cos(qt)]. \tag{20}$$

Substituting Eq. (20) in Eq. (18), the Green's function $G_{bb}(t)$ takes up the form:

$$G_{bb}(t) = -i e^{-it(-E_b)} \times \exp\left[- \sum_q \frac{2 g_{bb}^2 \xi^2 T}{q^3} [1 - \cos(qt)] \right]. \tag{21}$$

In the continuum limit, we obtain

$$G_{bb}(t) = -i e^{itE_b} \times \exp\left[- 2 g_{bb}^2 T \int_\epsilon^{\omega_D} \left[\frac{1 - \cos(qt)}{q^3} \right] \mathrm{d}q \right]. \tag{22}$$

The integral in Eq. (22) can be expressed in terms of known functions

$$\int_\epsilon^{\omega_D} \frac{[1 - \cos(qt)]}{q^3} \mathrm{d}q = -\frac{1}{2q^2} + \frac{\cos(qt)}{2q^2} + \frac{1}{2} t^2 \mathrm{Ci}(qt) - \frac{t \sin(qt)}{2q} \Big|_\epsilon^{\omega_D}, \tag{23}$$

where the function $\mathrm{Ci}(x)$ has the following expansion [26] for $x \ll 1$,

$$\mathrm{Ci}(x) = \gamma + \log|x| + \sum_{n=1}^{\infty} \frac{(-1)^n x^{2n}}{2n(2n)!}$$

and γ is the Euler-Mascheroni constant.

The integrand of Eq. (23) oscillates and decays rapidly with increasing q, so the contribution at the upper limit of integration is negligible (especially since $\omega_D/\epsilon \gg 1$). The exponentiated function which appears in Eq. (22) oscillates as a function of time around the constant value $\exp(-g_{bb}^2 T/\epsilon^2)$ which is due to the first term on the right-hand side of Eq. (23). This number is vanishingly small for all reasonable values of the cutoff and the other constants.

Next, we take the Fourier transform of Eq. (22),

$$G_{bb}(E + E_b) = -i \int_0^\infty dt e^{it(E+E_b)} \times \exp\left[- 2 g_{bb}^2 T \int_\epsilon^{\omega_D} \left[\frac{1 - \cos(qt)}{q^3} \right] dq \right]. \tag{24}$$

Before performing a full numerical evaluation, it is useful to estimate the decay of the envelope of oscillations. This can be done for large times, but subject to the limit $t \ll 1/\epsilon$ (keeping in mind that ϵ is small), so that in the integral the largest contribution comes from momenta $qt \ll 1$, and the logarithmic term dominates. In this case, Eq. (24) reduces to

$$G_{bb}(E + E_b) \approx -i \int_0^\infty \mathrm{d}t e^{i(E+E_b)t} \exp\left[- g_{bb}^2 T t^2 \log\left|\frac{1}{t\epsilon}\right| \right]. \tag{25}$$

In this regime, the oscillations are not visible. We see that for our model, the damping factor is given as $f(t) \approx \exp[-g_{bb}^2 T t^2 \log|1/(t\epsilon)|]$ which has a different structure than the case of 3D QED, where the damping factor is $f(t) \approx \exp[-\alpha T t \log(\omega_p t)]$ with ω_p and α being the plasma frequency and the fine structure constant [21].

Next, we consider the more general case and numerically integrate Eq. (24). We use the following transformation of variables: $(E + E_b)t = x$ and $q/(E + E_b) = y$ and under the approximation that $\omega_D \gg E_b, E$, we rewrite a nondimensional form of the bound state Green's function $\tilde{G}_{bb}$:

$$\tilde{G}_{bb}(\tilde{E}) = -\frac{i}{\sqrt{\lambda}}\int_0^\infty dx \frac{e^{ix}}{\tilde{E}} \times \exp\left[-\frac{1}{\tilde{E}^2}\int_{\frac{\omega_m}{\tilde{E}}}^\infty \left[\frac{1-\cos(yx)}{y^3}\right]dy\right]. \quad (26)$$

Here we define the dimensionless cutoff ω_m and energy $\tilde{E}$ in the following convenient way:

$$\lambda = 2g_{bb}^2 T, \quad \omega_m = \epsilon/\sqrt{\lambda}, \quad \tilde{E} = (E + E_b)/\sqrt{\lambda}\,. \quad (27)$$

The real and the imaginary parts of Eq. (26) are given as follows:

$$\mathrm{Re}\tilde{G}_{bb}(\tilde{E}) = \frac{1}{\sqrt{\lambda}}\int_0^\infty dx \frac{\sin(x)}{\tilde{E}} \times \exp\left[-\frac{1}{\tilde{E}^2}\int_{\frac{\omega_m}{\tilde{E}}}^\infty \left[\frac{1-\cos(yx)}{y^3}\right]dy\right] \quad (28)$$

$$\mathrm{Im}\tilde{G}_{bb}(\tilde{E}) = -\frac{1}{\sqrt{\lambda}}\int_0^\infty dx \frac{\cos(x)}{\tilde{E}} \times \exp\left[-\frac{1}{\tilde{E}^2}\int_{\frac{\omega_m}{\tilde{E}}}^\infty \left[\frac{1-\cos(yx)}{y^3}\right]dy\right]. \quad (29)$$

We choose parameters appropriate for a graphene membrane with a physisorption well $E_b = 40$ meV, $g_{bb}^2 = 60$ μeV, and $\omega_D = 65$ meV. The variation of the imaginary and the real parts of $\tilde{G}_{bb}$ with the dimensionless infrared frequency cutoff ω_m is captured in Figs. 6 and 7, respectively.

As discussed previously, there exists also a time-independent factor $\exp(-g_{bb}^2 T/\epsilon^2)$ that leads to a singular $\delta(\omega)$ function contribution with spectral weight $\exp(-1/2\omega_m^2)$ to the imaginary part. This contribution is not visible in Fig. 7

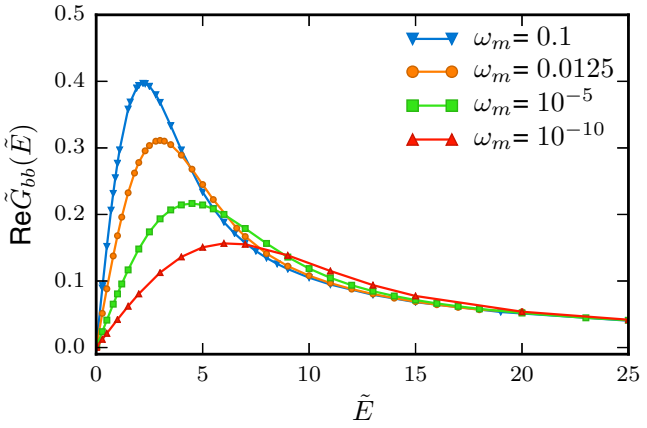

FIG. 6. Variation of the real part of the dimensionless Green's function in the bound state $\tilde{G}_{bb}$ for different values of the effective infrared cutoff ω_m.

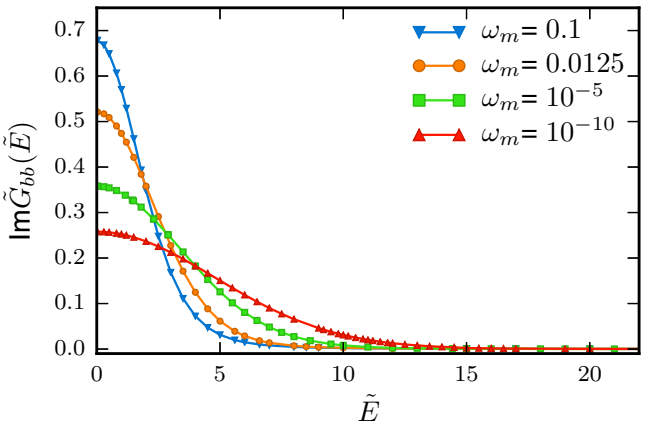

FIG. 7. The imaginary part of the (dimensionless) Green function in the bound state $\tilde{G}_{bb}$ vs energy $\tilde{E}$ for different values of the infrared cutoff ω_m.

since for the cutoff values used, the additional δ-function spectral weight is vanishingly small. It can however become appreciable upon further increase of ω_m beyond 0.2 or so, which would take us beyond the region of validity of our model.

We conclude that both real and imaginary parts are well behaved but still exhibit some infrared cutoff dependence. Most importantly, there is no quasiparticle pole and the Green's function is damped. The residual cutoff dependence reflects the low dimensionality of the membrane flexural fluctuations.

V. STICKING RATES

We use the numerically solved $\tilde{G}_{bb}$ to derive the renormalized 1-loop atom self-energy Σ_{kk}^r, which in turn is used to derive the sticking rate Γ of the cold atom on finite temperature graphene membranes. We recall, the rate of transition of the cold atom from the continuum state $|k\rangle$ to the bound state $|b\rangle$ is given as:

$$\Gamma = -2Z(E_k) Im\,\Sigma_{kk}(E_k), \quad (30)$$

where Z is the renormalization factor and is given as: $Z = [1 - (\partial \mathrm{Re}\Sigma_{kk}(E_k)/\partial E)]^{-1}$ and E_k is the initial atom energy, respectively.

From Eq. (5), we obtain the following expression for the atom self-energy:

$$\Sigma_{kk}^{(1)} = g_{kb}^2 T \int_\epsilon^{\omega_D} \left[\frac{1}{q}\tilde{G}_{bb}\left(\frac{E + E_b - q}{\sqrt{\lambda}}\right) + \frac{1}{q}\tilde{G}_{bb}\left(\frac{E + E_b + q}{\sqrt{\lambda}}\right)\right]\mathrm{d}q. \quad (31)$$

Our final results, summarized in Eqs. (30) and (31), reflect the idea that, in order to obtain numerically accurate results, is is sufficient to keep the lowest (first) order in the smallest coupling g_{kb}^2 while using the fully renormalized G_{bb} which contains all orders in the strong coupling g_{bb}^2.

We numerically integrate Eq. (31) for two different infrared cutoff frequencies which physically correspond to two different sizes of the graphene membrane. We consider 1 μm and 100 nm sizes. The velocity of flexural sound waves in

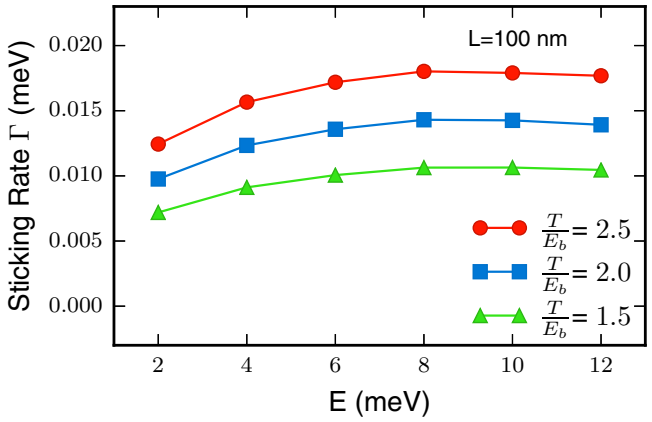

FIG. 8. The sticking rate $\Gamma(E)$ of the cold atom on graphene membrane ($L = 100$ nm), as a function of the initial atom kinetic energy E. An increase in Γ is observed for increasing temperature T of the membrane.

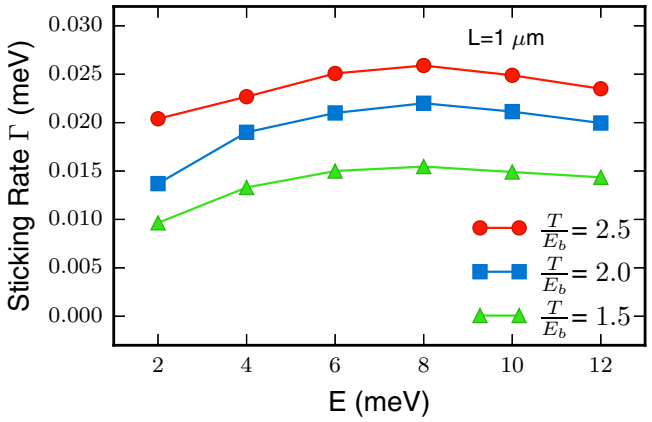

FIG. 9. For a membrane size of $L = 1$ μm, Γ is seen to increase even further with temperature T, which is an indication of the increasing damping of the atom wave function.

graphene is taken to be $v_s = \sqrt{\gamma/\sigma} = 6.64 \times 10^3$ m/s, where γ and σ are defined as the out-of plane membrane tension and membrane mass density for graphene [19,27,28], so that the physical cutoff corresponding to the two above mentioned membrane sizes are calculated as $\epsilon = 4.33 \times 10^{-3}$ meV and 0.043 meV, respectively.

It should be mentioned that anharmonic effects in the flexural phonon dispersion can become important as temperature increases, and they are a subject of current research [29–32]; however, if the tension γ is large enough such effects are naturally suppressed. The tension value we use from Refs. [15,19] is fairly large but lies in the border region where anharmonic corrections could become noticeable; detailed studies of such effects are beyond the scope of the present paper.

Now we present the numerical studies for the above-mentioned membrane sizes. For each membrane size, we calculate the dependence of Γ on temperature. For a membrane size of 100 nm, the dimensionless lower cutoff ω_m for the selected temperatures 1160 K, 928 K, and 696 K are given as 0.0125, 0.0141, and 0.01628, respectively. In Fig. 8 we see that the sticking rate increases with increasing temperature, a reflection of the physics of damping. A higher temperature corresponds to lower physical cutoff and hence a much broader curve of Im $\tilde{G}_{bb}$ (see Fig. 7). The broadening of the curve implies more damping and hence a higher decay rate. A similar trend is observed for the membrane size of 1 μm (Fig. 9) where ω_m are given as 0.00125, 0.001397, and 0.00163 for the above-mentioned temperatures.

For comparison, the transition rate can also be estimated using Fermi's golden rule (GR) for both in the zero-temperature and finite temperature cases. The golden rule is equivalent to first order in perturbation theory (in g_{kb}^2) and obviously does not contain the additional complex physics related to infrared effects discussed previously.

For the zero temperature case

$$\Gamma(T=0) = 2\pi \sum_f |\langle f|H_c|i\rangle|^2 \delta(E_f - E_i). \tag{32}$$

Here, we use the initial state and energy as: $|i\rangle = |k\rangle|0\rangle$ and $E_i = E_k$. The final state and energy is given as: $|f\rangle = |b\rangle|1_q\rangle$, $E_f = -E_{b0} + \omega_q$. The coupling term is given as $H_c = -g_{kb}(c_k^\dagger b + b^\dagger c_k)\sum_q \xi_q(a_q + a_q^\dagger) - g_{bb} b^\dagger b \sum_q \xi_q(a_q + a_q^\dagger)$. Therefore, in the continuum limit, the sticking rate Γ reduces to:

$$\Gamma_{GR}(T=0) = 2\pi g_{kb}^2. \tag{33}$$

Similarly, using the golden rule, an expression for Γ can be derived for finite temperature. For $T \gg E_{b0}$, we obtain

$$\Gamma_{GR}(T) = 2\pi \sum_f |\langle f|H_c|i\rangle|^2 \delta(E_f - E_i) N_q, \tag{34}$$

where N_q is the equilibrium phonon number. In the limit of $\omega_D \ll T$, we have $N_q \approx T/q$, and therefore:

$$\Gamma_{GR}(T) = 2\pi \sum_q g_{kb}^2 \xi^2 \delta(-E_{b0} + \omega_q - E_k)\frac{T}{q}. \tag{35}$$

In the continuum limit, we find the finite-temperature sticking rate from Fermi's golden rule as

$$\Gamma_{GR}(T) = \frac{2\pi g_{kb}^2 T}{(E_k + E_{b0})}. \tag{36}$$

We now compare the transition rates obtained from the golden rule both for zero and finite temperatures with the sticking rates obtained using $\tilde{G}_{bb}$ for the already mentioned ω_m. We see in Fig. 10 that the sticking rates derived by incorporating $\tilde{G}_{bb}$ are enhanced compared to the golden rule results, which is natural since it reflects additional damping arising from higher-order processes.

VI. SUMMARY AND DISCUSSION

In summary, we have considered the infrared dynamics of atoms interacting with a graphene membrane at finite temperature. This problem exhibits particularly severe infrared divergences order by order in perturbation theory, due to the singular nature of low-energy flexural phonon emission. Our model can be viewed as a two-channel generalization of the independent boson model, with a much weaker atom-phonon

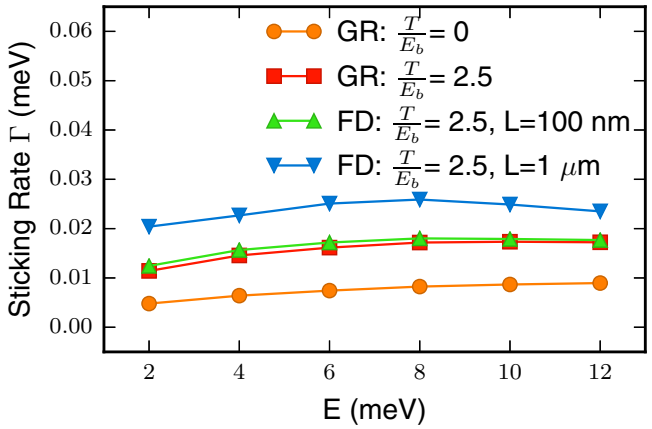

FIG. 10. With the increase in the cutoff ω_m (or decrease in the size of the membrane), the sticking rate Γ is seen to decrease. However, we anticipate that within our model Γ will not be smaller than the golden rule (GR) results derived for that specific temperature.

coupling constant in one of the channels relative to the other. This allows us to take advantage of the exact nonperturbative solution of the IBM in the stronger channel while treating the other one perturbatively. In the low-energy limit, the exact solution can be viewed as a resummation (exponentiation) of the most divergent diagrams in the perturbative expansion, which we have checked explicitly. As a result of this procedure we obtain the atom Green's function which we use to calculate the atom damping rate, in turn related to the quantum sticking rate. A characteristic feature of our results is that the Green's function retains some infrared cutoff dependence, which is relatively weak but still detectable by relating the infrared cutoff to the inverse membrane size. We provide detailed predictions for the sticking rate of H atoms as a function of temperature and size. Sticking is generally enhanced relative to the conventional Fermi golden rule result (which is equivalent to the lowest, 1-loop perturbative term) which is natural since higher order processes are required to increase damping at finite temperature. Although we observe an enhancement from the golden rule result, we still see the trend of decreasing sticking rates for low energies, contrary to some recent results, where numerical calculations predict an increased sticking rate with low incident energies [27].

It is also worth noticing, as we mention in the Introduction, that our approach is very similar in spirit to the calculation of fermion damping rates in "hot" QED and QCD, where the gauge structure of the theory is not particularly important as far as infrared properties are concerned. This problem has a long history, and the relevant theoretical approach, based on the finite temperature version of the Bloch-Nordsieck method, relies on exponentiation of infrared-divergent perturbation series (and is thus similar to the solution of the independent boson model in solid state theory.) The role of the long-range gauge propagator is played in our case by the phonon propagator. There are also important differences between our results and those in hot gauge theories. One difference, which has experimental consequences for the damping rate, is the residual dependence on the infrared cutoff, which can be traced to the quasi-1D nature of our problem (in the sense that a normally incident atom excites only axisymmetric flexural phonons). On the other hand, our perturbative expansion does not contain any polarization loop corrections (which are important ingredients of hot gauge theories), since in the case of a single atom interacting with phonon bath, those are completely absent from the theory.

We envisage applications of our approach to related physical systems, such as graphene under additional uniaxial strain, and other atomically thin materials, for example dichalcogenides and similar systems. In these materials various types of strain are expected to exist [33], as well as larger (compared to graphene) spin-orbit interactions. Additional uniaxial strain, for example, also affects strongly the van der Waals potential near the surface [34]. Therefore the atom damping rate is expected to be very sensitive to the physical characteristics of the atom-surface interactions, such as the strain-modified shape of the phonon flexural modes and the van der Waals interactions between atoms and surfaces which determine the bound state energies and corresponding atom-phonon coupling parameters.

ACKNOWLEDGMENTS

S.S. would like to thank Nathan S. Nichols and Adrian Del Maestro for their help with the figures in the paper. The research of V.N.K. was supported by the U.S. Department of Energy (DOE) Grant No. DE-FG02-08ER46512.

APPENDIX A: 2-LOOP ATOM SELF-ENERGY

Here we calculate the 2-loop atom self-energy corresponding to the diagrams shown in Fig. 11. These are the leading diagrams with two loops which reflect the change of the self-energy in the open k channel due to the influence of the b channel.

We begin our calculation by deriving an analytical expression for the vertex function $\Gamma(E,\omega)$ which is given by a diagram topologically similar to Fig. 5, but in the kb channel:

$$\Gamma(E,\omega) = i g_{bb}^2 \xi^2 g_{kb} \xi \sum_q \int \frac{d\omega'}{2\pi} \frac{T}{\omega_q} (-2\pi i) \Big[\delta(\omega' - \omega_q) + \delta(\omega' + \omega_q) \Big] \times \Big[\frac{1}{[E + E_{b0} - \omega' + i\eta]} \times \frac{1}{[E + E_{b0} - \omega - \omega' + i\eta]} \Big]. \quad \text{(A1)}$$

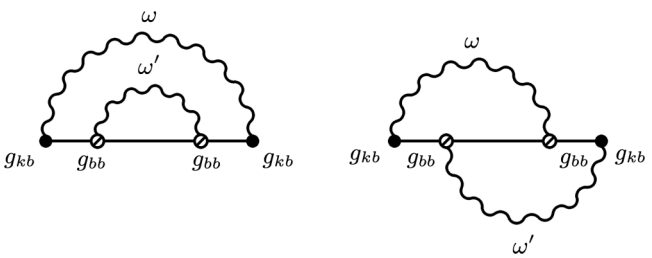

FIG. 11. 2-loop atom self-energy diagrams: rainbow (left) and vertex correction (right).

In the continuum limit, we have,

$$\Gamma(E,\omega) = g_{bb}^2\xi^2 g_{kb}\xi\rho_0 \int_{\epsilon}^{E+E_{b0}} \left[\frac{1}{(E+E_{b0}-q)} \times \frac{1}{(E+E_{b0}-\omega-q+i\eta)} + \frac{1}{(E+E_{b0}+q)(E+E_{b0}-\omega+q+i\eta)}\right]\frac{dq}{q}. \tag{A2}$$

Under the approximation, $q \ll E+E_{b0}$ and calling $g_{bb}^2\xi^2\rho_0 \to g_{bb}^2$, the real and the imaginary parts of the vertex function $\Gamma(E,\omega)$ are written as:

$$\mathrm{Re}\Gamma(E,\omega) = \frac{2g_{bb}^2 T g_{kb}\xi}{(E+E_{b0})(E+E_{b0}-\omega)} \log\left|\frac{E+E_{b0}}{\epsilon}\right|. \tag{A3}$$

Similarly, the imaginary part is given as

$$\mathrm{Im}\Gamma(E,\omega) = -\frac{\pi g_{bb}^2 T g_{kb}\xi}{(E+E_{b0})(E+E_{b0}-\omega)}. \tag{A4}$$

Using the vertex function $\Gamma(E,\omega)$, we derive the contribution from the vertex-corrected self-energy first. The analytical expression can be written as

$$\Sigma_{kk}^{(2)} = i g_{kb}\xi \int \frac{d\omega}{2\pi} G_{bb}(E-\omega)\Gamma(E,\omega)D^{<}(\omega). \tag{A5}$$

Performing the calculation, we find an expression for the real part of $\Sigma_{kk}^{(2)}$:

$$\mathrm{Re}\Sigma_{kk}^{(2)} = \frac{2g_{kb}^2 g_{bb}^2 T^2}{(E+E_{b0})^3}\left[\log\left|\frac{E+E_{b0}}{\epsilon}\right|\right]^2. \tag{A6}$$

A similar expression is derived for the contribution from the rainbow diagram. Thus, the above calculations show that the real part of Σ_{kk} at two-loop order is log squared infrared divergent.

APPENDIX B: VERTEX RENORMALIZATION

Now we calculate the vertex renormalization for the two different types of vertices in our model. The one loop vertex diagrams are shown in Fig. 12.

The corrections to the vertices are represented as $(g_{kb} + \delta\Gamma_{kb}^{(1)})$ and $(g_{bb} + \delta\Gamma_{kb}^{(1)})$. By evaluating the corresponding diagrams we obtain for the infrared-divergent parts:

$$\delta\Gamma_{kb}^{(1)}(E) = -\frac{g_{kb}^3 T}{\pi(E+E_{b0})^2}\log\left|\frac{E+E_{b0}}{\epsilon}\right|, \tag{B1}$$

$$\delta\Gamma_{bb}^{(1)}(E) = \frac{g_{bb}^3 T}{\pi(E+E_{b0})^2}\log\left|\frac{E+E_{b0}}{\epsilon}\right|. \tag{B2}$$

Here, the external phonon frequency is set to zero (infrared limit), while E is the external atom energy. The most important feature of these results is that the corrections have different signs, i.e., while the kb vertex decreases, the bb vertex increases.

It is possible to write down and solve the corresponding Dyson equations for the fully renormalized vertex functions, which is equivalent to summing an infinite series of ladder diagrams as is conventionally done in QED [35]. This results in the following expressions for the effective vertices in the two channels:

$$\Gamma_{kb}(E) = \frac{g_{kb}}{1+\frac{g_{kb}^2 T}{\pi(E+E_{b0})^2}\log\left|\frac{E+E_{b0}}{\epsilon}\right|}, \tag{B3}$$

and

$$\Gamma_{bb}(E) = \frac{g_{bb}}{1-\frac{g_{bb}^2 T}{\pi(E+E_{b0})^2}\log\left|\frac{E+E_{b0}}{\epsilon}\right|}. \tag{B4}$$

Again, it is clear that $\Gamma_{kb}(E)$ decreases while $\Gamma_{bb}(E)$ increases in the infrared limit. $\Gamma_{bb}(E)$ in fact contains a Landau pole, although due to the smallness of the effective coupling, the system never reaches the pole for physical values of the parameters (coupling, temperature, and cutoff).

Finally, we consider even higher order renormalization effects. For the kb vertex, the next level of complexity is represented by the crossed vertex corrections shown in Fig. 13. By evaluating the diagram we obtain

$$\delta\Gamma_{kb}^{(2)}(E) = -\frac{2g_{kb}^3 g_{bb}^2 T^2}{\pi^2(E+E_{b0})^4}\log^2\left|\frac{E+E_{b0}}{\epsilon}\right|, \tag{B5}$$

which confirms that the kb vertex keeps decreasing. Corresponding results can be derived for the bb vertex (which experiences an increase). These results are conceptually important because they reaffirm the different tendencies in the two channels, although numerically these diagrams are very small for physical parameter values.

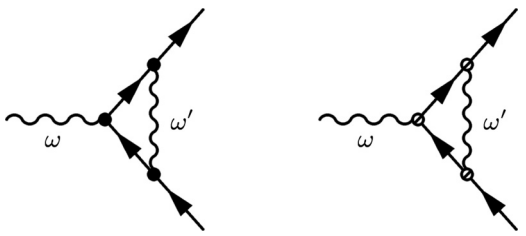

FIG. 12. Vertex diagrams corresponding to transitions from: $|k\rangle \to |b\rangle$ states (left), and $|b\rangle \to |b\rangle$ states (right).

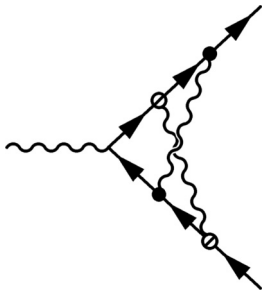

FIG. 13. Higher order crossed vertex corrections to the kb vertex.

[1] A. G. Manning, R. Khakimov, R. G. Dall, and A. G. Truscott, Phys. Rev. Lett. **113**, 130403 (2014).

[2] M. Nielsen and I. Chuang, *Quantum Computation and Quantum Information* (Cambridge University Press, Cambridge, England, 2004).

[3] J. D. Thompson, T. G. Tiecke, N. P. de Leon, J. Feist, A. V. Akimov, M. Gullans, A. S. Zibrov, V. Vuletic, and M. D. Lukin, Science **340**, 1202 (2013).

[4] F.-X. Esnault, E. Blanshan, E. N. Ivanov, R. E. Scholten, J. Kitching, and E. A. Donley, Phys. Rev. A **88**, 042120 (2013).

[5] J. A. Sedlacek, E. Kim, S. T. Rittenhouse, P. F. Weck, H. R. Sadeghpour, and J. P. Shaffer, Phys. Rev. Lett. **116**, 133201 (2016).

[6] A. D. Cronin, J. Schmiedmayer, and D. E. Pritchard, Rev. Mod. Phys. **81**, 1051 (2009).

[7] B. Segev, R. Côté, and M. G. Raizen, Phys. Rev. A **56**, R3350 (1997).

[8] J. Fortágh and C. Zimmermann, Rev. Mod. Phys. **79**, 235 (2007).

[9] J. E. Lennard-Jones and A. F. Devonshire, Proc. R. Soc. London A **156**, 29 (1936).

[10] D. P. Clougherty and W. Kohn, Phys. Rev. B **46**, 4921 (1992).

[11] Y. Zhang and D. P. Clougherty, Phys. Rev. Lett. **108**, 173202 (2012).

[12] D. P. Clougherty and Y. Zhang, Phys. Rev. Lett. **109**, 120401 (2012).

[13] N. D. Mermin, Phys. Rev. **176**, 250 (1968).

[14] D. P. Clougherty, Phys. Rev. Lett. **113**, 069601 (2014).

[15] B. Lepetit and B. Jackson, Phys. Rev. Lett. **107**, 236102 (2011).

[16] J. F. Annett and P. M. Echenique, Phys. Rev. B **36**, 8986 (1987).

[17] R. D. Williams, M. W. Cole, and S. E. Koonin, Phys. Rev. B **28**, 1076 (1983).

[18] E. R. Bittner and J. C. Light, J. Chem. Phys. **102**, 2614 (1995).

[19] D. P. Clougherty, Phys. Rev. B **90**, 245412 (2014).

[20] G. D. Mahan, *Many-Particle Physics* (Plenum Press, New York, 1981).

[21] J.-P. Blaizot and E. Iancu, Phys. Rev. D **55**, 973 (1997).

[22] J.-P. Blaizot and E. Iancu, Phys. Rev. D **56**, 7877 (1997).

[23] J.-P. Blaizot and E. Iancu, Phys. Rep. **359**, 355 (2002).

[24] V. Lebedev and A. Smilga, Ann. Phys. **202**, 229 (1990).

[25] E. M. Lifshitz and L. P. Pitaevskii, *Physical Kinetics (Landau and Lifshitz Vol. 10)* (Pergamon Press, Oxford, England, 1981).

[26] M. Abramowitz and I. Stegun, *Handbook of Mathematical Functions with Formulas, Graphs and Mathematical Tables* (Dover, New York, 1964).

[27] B. Lepetit and B. Jackson, Phys. Rev. Lett. **113**, 069602 (2014).

[28] K. H. Michel and B. Verberck, Phys. Rev. B **78**, 085424 (2008).

[29] M. I. Katsnelson and A. Fasolino, Acc. Chem. Res. **46**, 97 (2013).

[30] B. Amorim, R. Roldán, E. Cappelluti, A. Fasolino, F. Guinea, and M. I. Katsnelson, Phys. Rev. B **89**, 224307 (2014).

[31] K. V. Zakharchenko, M. I. Katsnelson, and A. Fasolino, Phys. Rev. Lett. **102**, 046808 (2009).

[32] R. Roldán, A. Fasolino, K. V. Zakharchenko, and M. I. Katsnelson, Phys. Rev. B **83**, 174104 (2011).

[33] B. Amorim, A. Cortijo, F. de Juan, A. Grushin, F. Guinea, A. Gutiérrez-Rubio, H. Ochoa, V. Parente, R. Roldán, P. San-Jose, J. Schiefele, M. Sturla, and M. Vozmediano, Phys. Rep. **617**, 1 (2016).

[34] N. S. Nichols, A. D. Maestro, C. Wexler, and V. N. Kotov, Phys. Rev. B **93**, 205412 (2016).

[35] V. B. Berestetskii, E. M. Lifshitz, and L. P. Pitaevskii, *Quantum Electrodynamics (Landau and Lifshitz Vol. 4)* (Butterworth-Heinemann, England, 1982).